2019

Hydrogen-Containing Na3HTi1- xMnxF8 Narrow-Band Phosphor for Light-Emitting Diodes

Muhuai Fang
National Taiwan University

Tsun Yang
National Taipei University of Technology

Tadeusz Lesniewski
University of Gdansk, Poland

Chi Lee
National Taiwan University

Sebastian Mahlik
University of Gdansk, Poland

See next page for additional authors

Publication Details

Fang, M., Yang, T., Lesniewski, T., Lee, C., Mahlik, S., Grinberg, M., Peterson, V. K., Didier, C., Pang, W., Su, C. & Liu, R. (2019). Hydrogen-Containing Na3HTi1- xMnxF8 Narrow-Band Phosphor for Light-Emitting Diodes. ACS Energy Letters, 4 (2), 527-533.

Hydrogen-Containing Na3HTi1- xMnxF8 Narrow-Band Phosphor for Light-Emitting Diodes

Abstract

We synthesize the phosphor $Na_3HTi_{1-x}Mn_xF_8$ ($Na_3HTiF_8:Mn^{4+}$) material series using a coprecipitation method. We determine the complete phase and crystallographic structure of the Na_3HTiF_8 series end-member, including the determination of the H atoms at the 4b (0, 1/2, 0) crystallographic site within the Cmcm space group symmetry structure, resulting in a quantum efficiency of ~44%, which is comparative to the $Na_2SiF_6:Mn^{4+}$ phosphor materials. We successfully model the luminescent properties of the $Na_3HTi_{1-x}Mn_xF_8$ material series, including temperature and time-dependent photoluminescence, providing a good prediction of the decay properties at low and high temperature and revealing the existence of Mn^{5+} during the ionization process. Notably, LED package data indicates that the $Na_3HTi_{1-x}MnxF_8$ material series could be a promising candidate for high-level and back-lighting devices. This research reveals the role that hydrogen plays in determining fluoride phosphor structure and properties, revealing a new path for the synthesis of fluoride phosphors.

Disciplines

Engineering | Physical Sciences and Mathematics

Publication Details

Fang, M., Yang, T., Lesniewski, T., Lee, C., Mahlik, S., Grinberg, M., Peterson, V. K., Didier, C., Pang, W., Su, C. & Liu, R. (2019). Hydrogen-Containing Na3HTi1- xMnxF8 Narrow-Band Phosphor for Light-Emitting Diodes. ACS Energy Letters, 4 (2), 527-533.

Authors

Muhuai Fang, Tsun Yang, Tadeusz Lesniewski, Chi Lee, Sebastian Mahlik, Marek Grinberg, Vanessa K. Peterson, Christophe R. Didier, Wei Kong Pang, Chaochin Su, and Ru-Shi Liu

Published as:
Fang, M., Yang, T., Lesniewski, T., Lee, C., Mahlik, S., Grinberg, M., Peterson, V. K., Didier, C., Pang, W., Su, C. & Liu, R. (2019). Hydrogen-Containing Na3HTi1- xMnxF8 Narrow-Band Phosphor for Light-Emitting Diodes. *ACS Energy Letters, 4 (2)*, 527-533.

Hydrogen Containing $Na_3HTi_{1-x}Mn_xF_8$ Narrow-Band Phosphor for Light Emitting Diodes

Mu-Huai Fang,[†] Tsun-Hsiung Yang,[‡] Tadeusz Lesniewski,[§] Chi Lee,[†] Sebastian Mahlik,[§] Marek Grinberg,[§] Vanessa K. Peterson[&,#], Christophe Didier[&,#], Wei Kong Pang,[*,#] Chaochin Su,[*,‡] and Ru-Shi Liu[*,†,⊥]

[†]Department of Chemistry, National Taiwan University, Taipei 106, Taiwan
[‡]Institute of Organic and Polymeric Materials, National Taipei University of Technology, Taipei 10608, Taiwan
[§]Institute of Experimental Physics, Faculty of Mathematic, Physics and Informatics, Gdańsk University, Wita Stwosza 57, 80-308 Gdańsk, Poland
[&]Australian Centre for Neutron Scattering, Australian Nuclear Science and Technology Organisation, Locked Bag 2001, Kirrawee DC, NSW, 2232, Australia
[#]Institute for Superconducting & Electronic Materials, University of Wollongong, NSW 2522, Australia
[⊥]Department of Mechanical Engineering and Graduate Institute of Manufacturing Technology, National Taipei University of Technology, Taipei 106, Taiwan

Corresponding Authors

* wkpang@uow.edu.au

* f10913@ntut.edu.tw

* rsliu@ntu.edu.tw

ABSTRACT

We synthesize the phosphor $Na_3HTi_{1-x}Mn_xF_8$ ($Na_3HTiF_8:Mn^{4+}$) material series using a co-precipitation method. We determine the complete phase and crystallographic structure of the Na_3HTiF_8 series end-member, including the determination of the H atoms at the 4b (0, 1/2, 0) crystallographic site within the *Cmcm* space group symmetry structure, resulting in a quantum

efficiency of ~ 44%, which is comparative to the $Na_2SiF_6:Mn^{4+}$ phosphor materials. We successfully model the luminescent properties of the $Na_3HTi_{1-x}Mn_xF_8$ material series, including temperature and time-dependent photoluminescence, providing a good prediction of the decay properties at low and high temperature, and revealing the existence of Mn^{5+} during the ionization process. Notably, LED package data indicates that the $Na_3HTi_{1-x}Mn_xF_8$ material series could be a promising candidate for high-level and back lighting devices. This research reveals the role that hydrogen plays in determining fluoride phosphor structure and properties, revealing a new path for the synthesis of fluoride phosphors.

TOC GRAPHICS

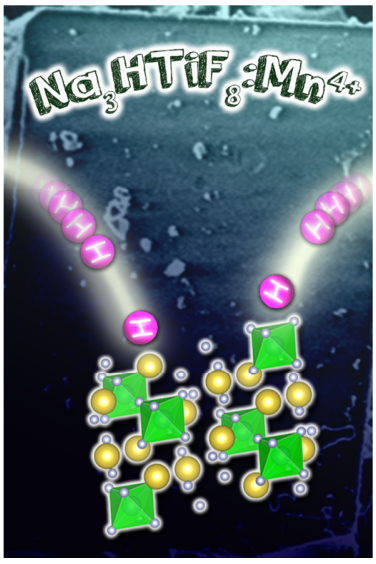

White light-emitting diodes (LEDs) are eco-friendly, affordable, and have high efficiency. Phosphor, as a matrix material for controlling the luminescent color of LED devices, has become a field of interest,[1-4] with Mn^{4+}-doped phosphors in particular gaining attention as a result of being rare-earth-free and having relatively narrow band emission spectra. Amongst host

phosphors, Mn^{4+}-doped fluorides can generate a red emission with an emission peak ~ 630 nm, beneficial for high-level back lighting devices. The narrow-emission of these materials avoids the substantial energy losses at wavelengths beyond 650 nm that occurs in traditional red phosphor materials, such as $CaAlSiN_3:Eu^{2+}$ and $Sr_2Si_5N_8:Eu^{2+}$.[5-7] Therefore, Mn^{4+}-doped fluorides have sharp emissions over adequate luminescent wavelengths leading to zero-waste photon ratios.[8] Accordingly, efforts have focused on synthesis methods for such materials, including the synthesis of Mn^{4+}-doped fluoride phosphors using wet chemical etching[9-13] and the development of cation-exchange methods to synthesize the $K_2TiF_6:Mn^{4+}$ phosphor, resulting in enhanced quantum efficiency and luminous efficacy of LED devices.[14] The most common synthetic approach being co-precipitation using two solutions that are mixed to obtain a Mn^{4+}-doped fluoride phosphor.[15-16] Most fluoride phosphors synthesized to date belong to the chemical composition $A_2MF_6:Mn^{4+}$, $BMF_6:Mn^{4+}$, and $D_3MF_7:Mn^{4+}$ (A = NH_4^+, Li^+, Na^+, K^+, Rb^+, Cs^+, B = Mg^{2+}, Ca^{2+}, Sr^{2+}, Ba^{2+} , D = Zr and M = Si, Ge, Zr, Sn, Ti). A major drawback of the co-precipitation method is the limitation of the species of the host material, which has limited the development of fluoride phosphors and consequently, the development of the luminescence properties of Mn^{4+} in more complicated structures. By contrast, cation exchange is a relatively-easy method of synthesizing a Mn^{4+}-doped phosphor in a specified material. Although more diverse host materials can be produced in this way, the lower quantum efficiencies of materials produced by cation-exchange compared to co-precipitation methods limit the practical application of cation-exchange produced materials in white LEDs.

In this study, we synthesize the novel $Na_3HTi_{1-x}Mn_xF_8$ ($Na_3HTiF_8:Mn^{4+}$) material series using a modified co-precipitation method. High-resolution neutron powder diffraction (NPD) is used to comprehensively characterize and determine the complete crystallographic details of the

Na_3HTiF_8 end-member material, which we use a basis for understanding the luminescent properties of the Mn^{4+} phosphor series that we measure, where LED package data showing promise of the material series for high-level back lighting devices.

Energy dispersive spectroscopy (EDS) of $Na_3HTi_{0.95}Mn_{0.05}F_8$ sample was performed (Figure S1) and confirmed a Na:Ti ratio of 22:7.7, in close agreement to the expected composition. X-ray powder diffraction with D2-phaser of the as-prepared Na_3HTiF_8:Mn^{4+} samples (Figure 1a) produced similar results across the series and could not provide information concerning the location of H atoms (not previously determined for the parent Na_3HTiF_8 material in ICSD#14131). The determination of H within the structure, which influences the electronic environment of F and therefore the bandgap, was performed using high-resolution NPD. Full Rietveld analysis using these data confirmed a main phase of orthorhombic Na_3HTiF_8 and secondary phase of tetragonal Na_2TiF_6 in the parent Na_3HTiF_8 material, able to be described using the structures in ICSD#14131 and #24477 as starting structures, respectively, resulting in a final refined weight fraction of 63:37. The coherent neutron scattering length of the H nucleus (-0.3742 x 10^{-12} cm) makes it straightforward to obtain a quantitative refinement of the structural model for the material that includes H, with Refinement profiles for models without and with H shown in Figure 1b and c, respectively. In the model without H, the residual negative nuclear density arising from H in the structure can clearly be observed and a model that includes H at the (0, 1/2, 0) 4*b* crystallographic site refined from this (Figure 1d and Table S1). Following the inclusion of the H into the orthorhombic phase model, the weight ratio of the orthorhombic and tetragonal phases was 58.7(7):41.3(7). Further, the inclusion of the H atom into the Na_3HTiF_8 structure leads to the distortion of the TiF_6^{2-} octahedral units due to the extra bonding in the structure. Besides, the HF bond is quite strong, which will also cause the distortion of the TiF_6^{2-}

octahedral units. As a result, this effect may contribute to the enhancement of the zero-phonon line. According to our previous study, if we define the distortion of $Na_2TiF_6:Mn^{4+}$ as 100%, $Na_3HTi_{1-x}Mn_xF_8$ possesses around 40% of the distortion of $Na_2TiF_6:Mn^{4+}$.[17] Morphology of these phosphor materials is known to affect luminescent intensity, with large and well-ordered crystallites usually resulting in high luminescent intensity as a result of reduced surface defect concentration. Scanning electron microscopy (SEM) images of $Na_3HTi_{0.95}Mn_{0.05}F_8$ (Figure S2) reveals high crystallinity, with an unusual appearance for fluoride phosphors that is indicative of decreased surface defects and consistent with enhanced photoluminescence intensity.

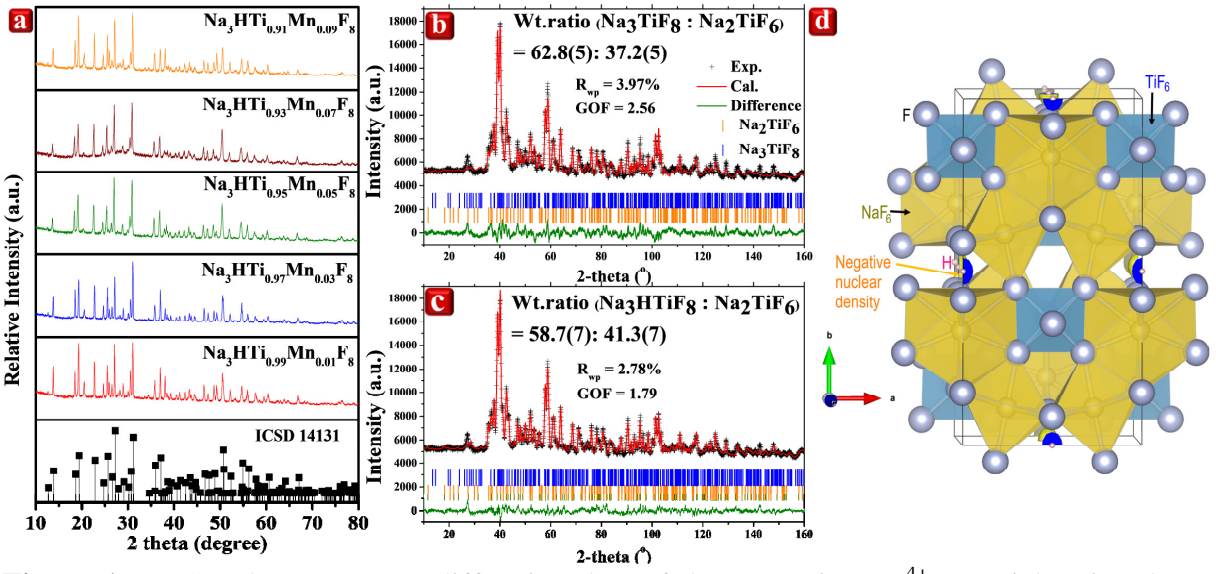

Figure 1. (a) Synchrotron X-ray diffraction data of the $Na_3HTiF_8:Mn^{4+}$ material series shown alongside the ICSD#14131 entry for the parent Na_3HTiF_8 material. (b) Rietveld refinement profiles of Na_3HTiF_8 using high-resolution NPD data using a structural model without (b) and with (c) H. (d) The Na_3HTiF_8 structure obtained from (c), overlaid with the Fourier-difference map obtained from (b) revealing negative nuclear density (yellow shell and blue inner) arising from H.

Photoluminescence (PL) and photoluminescence excitation (PLE) spectra of the $Na_3HTiF_8:Mn^{4+}$ series are shown in Figure 2a. The Na_3HTiF_8: Mn^{4+} series can be excited at 350 and 460 nm, corresponding to the spin-allowed $^4A_2 \rightarrow {}^4T_1$ and $^4A_2 \rightarrow {}^4T_2$ electron transitions, respectively, indicating efficient excitation by the blue LED. The PL spectra exhibit a sharp-line

emission and spin-forbidden $^2E \rightarrow {}^4A_2$ electron transition with a peak at ~ 627 nm, containing a zero-phonon line (ZPL) at 618 nm and lines related to phonon-assisted transitions. These spectra suggest the materials to be good candidates for LED devices as a result of the zero-waste photon ratios corresponding to photon ratios longer and shorter than 650 nm. Moreover, the zero-phonon line (ZPL) gains some intensity at around 618 nm, which indicates sensitivity to the local-coordination environment of Mn^{4+}. The hydrogen-free crystal structure has octahedral 6 coordinate Ti and Mn^{4+}, which is modified in the Na_3HTiF_8:Mn^{4+} series by the introduction of octahedral distortion of this unit, which is expected to impact the ZPL. Accordingly, the PL spectra for the Na_3HTiF_8:Mn^{4+} series show luminescent intensity reaching maximum 5% and 7% Mn^{4+}, before reducing at higher Mn levels. The internal quantum efficiency (IQE), absorption (abs.), and external quantum efficiency (EQE) are shown in Table S2, revealing that the 5% Mn^{4+} sample have the highest EQE, of 43.8%, comparable to that of the Na_2TiF_6:Mn^{4+} series of materials.The energy levels of the octahedrally coordinated Mn^{4+} are illustrated by the Tanabe-Sugano diagram (Figure 2b) showing ligand field splitting energies of localized states of the ion with respect to the crystal field strength $10Dq$.[17] The energetic structure of the $3d^3$ system is described quantitatively by the Racach parameters B and C and by the crystal field strength $10Dq$.[19-20]

$$B = \frac{\frac{(\Delta E)^2}{Dq} - 10\Delta E}{15(\frac{\Delta E}{Dq} - 8)} \quad (1)$$

where δE is the difference between the energy of the lowest $^4T_{1g}$ and $^4T_{2g}$ states. Value of C can be calculated from the equation:

$$\frac{E(\,^2E_g)}{B} = 3.05\frac{C}{B} + 7.9 - 1.8\frac{B}{Dq} \quad (2)$$

To analyze the emission lifetime, we considered the configurational coordinate diagram for electrons in Mn^{4+} in octahedral and distorted octahedral configurations in Figure 2c, where Q is the configurational coordinate, which can be considered as the distance between the central ion and ligands. The potential energy curves have minima at Q_E for ground ($^4A_{2g}$) and excited (^2E_g) states and are shifted in energy by value E(^2E_g). In the $^4T_{2g}$ state the parabola has a minimum at Q = Q_T and energy equal to $10Dq - S\hbar\omega$, where S is the Huang–Rhys factor and $\hbar\omega$ is the energy of local vibration mode. [17] Energy Δ is defined as the energetic distance between the minima of the $^4T_{2g}$ and ^2E_g electronic states. Energy Δ' is defined as the difference between the $^4T_{2g}$ and ^2E_g states for Q = Q_E (see Figure 2c). These parameters are listed in Table S3.

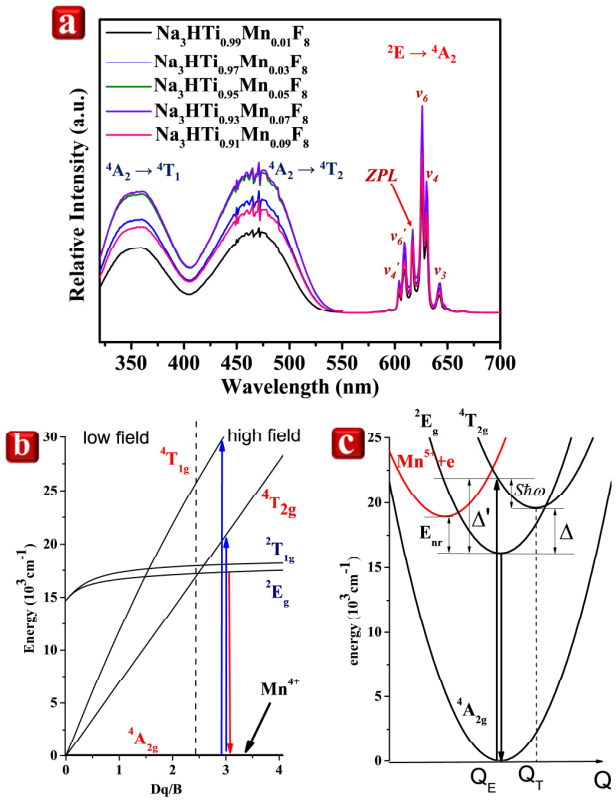

Figure 2. (a) Photoluminescence spectra of the $Na_3HTiF_8:Mn^{4+}$ series. (b) Tanabe–Sugano diagram for the $3d^3$ system. (c) Potential energy surface of the Mn^{4+} system where Q_E describes the position of F^- when electrons in Mn^{4+} occupy the $^4A_{2g}$ and ^2E_g states belonging to the t^3 electronic configuration and Q_T represents the positions of F^- when the system is in the $^4T_{2g}$ state.

The PL spectra of the $Na_3HTiF_8:Mn^{4+}$ series over 10–350 K are presented in Figure 3a. The emission spectra show the usual temperature-dependent increase of the anti-Stokes phonon lines ν_6' and ν_4', accompanied by a smaller increases of the Stokes phonon lines with energies $h\nu_3 = \hbar\omega_3 = 657$ cm^{-1}, $h\nu_4 = \hbar\omega_4 = 333$ cm^{-1}, and $h\nu_6 = \hbar\omega_6 = 214$ cm^{-1}, with respect to the ZPL. Evidence of splitting of the ZPL can be seen from the PL spectra below 200 K.

Figure 3b contains the temperature-dependent intensity ratio of Stokes and anti-Stokes sidebands to the ZPL emission intensity, obtained from their integrated areas in the PL spectra. The ratio of the Stokes and anti-Stokes line intensity (I_{S+A}) to the ZPL intensity (I_{ZPL}) is described by:[21]

$$\frac{(I_{S+A})}{I_{ZPL}} = \sum_v \frac{\Omega_{dyn}^2(v)}{\Omega_{stat}^2} \coth\left(\frac{\hbar\omega_v}{2kT}\right) \quad (3)$$

where k is the Boltzmann constant, T is temperature, $\hbar\omega_v$ is the energy of the v^{th} vibrational mode. The quantities Ω_{stat}^2 and $\Omega_{dyn}^2(v)$ are the effective dipole transition moments related to static distortions and distortion created by interaction with the v^{th} vibrational mode, respectively. The intensity of the ZPL appears temperature independent and is equal to the strength of interaction with the odd parity lattice distortion. Therefore the ratio $\Omega_{dyn}^2(v)/\Omega_{stat}^2$ can be obtained from the ratio of the integrated intensities of spectral lines in the low temperature experimental spectra, with these parameters presented in Table S4.

The increase of transition probability causes a decrease in the luminescence lifetime (τ), as shown by:

$$\tau(T) = \frac{\tau_0}{1+\sum_v \frac{\Omega_{dyn}^2(v)}{\Omega_{stat}^2} \coth\left(\frac{\hbar\omega_v}{2kT}\right)} \quad (3a)$$

where τ_0 is the lifetime of the ^2E_g state at low temperatures (10K). The temperature dependence of I_{S+A}/I_{ZPL} obtained using the relation (3) using data from Table S4 is shown by the solid curve in Figure 3b. The I_{S+A}/I_{ZPL} reproduces $\Omega^2_{dyn}(v)/\Omega^2_{stat}$ and we model this to understand the physical processes that lead to the appearance of the sharp line phonon sideband. We apply a simplified model in which real phonons are represented by a single phonon mode, and perform additional fitting using:

$$\frac{(I_{S+A})}{I_{ZPL}} = \frac{\Omega^2_{dyn}}{\Omega^2_{stat}} \coth\left(\frac{\hbar\omega_{eff}}{2kT}\right) \quad (4)$$

We obtain $\frac{\Omega^2_{dyn}}{\Omega^2_{stat}}$ = 5.7 and an effective phonon energy equal to $\hbar\omega_{eff}$=265 cm^{-1}, as presented by the dashed red curve in Figure 3b, which reproduces the experimental data well.

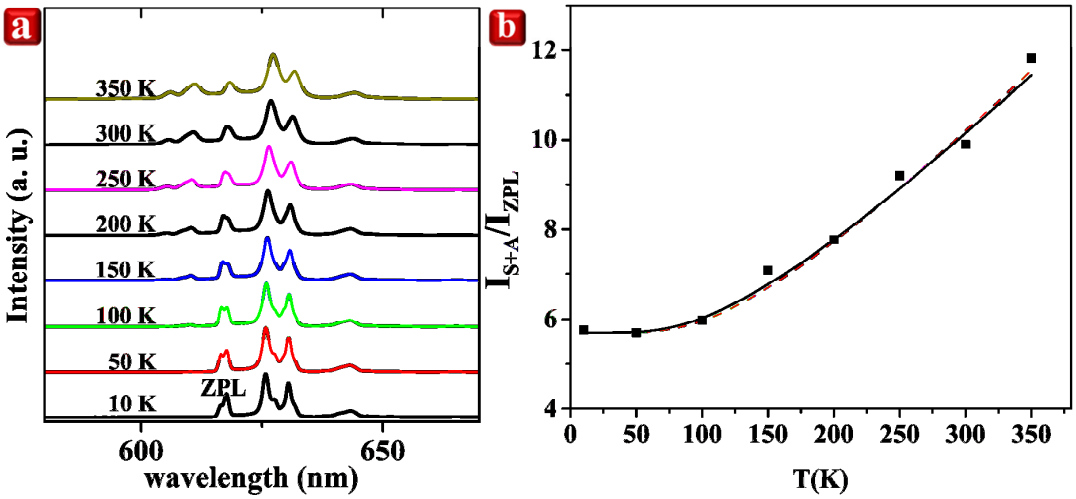

Figure 3. (a) Temperature dependence of PL spectra of the Na_3HTiF_8:Mn^{4+} series under excitation at 442 nm. (b) Ratio of the intensity of Stokes and anti-Stokes lines (I_{S+A}) to the intensity of the ZPL (I_{ZPL}) (solid line) and $\Omega^2_{dyn}(v)/\Omega^2_{stat}$ obtained from Table S4 (points) shown alongside the model (red dashes).

Figure 4a shows the temperature-dependent ZPL decay curves under 440 nm pulsed excitation where the points in Figure 4b correspond to the temperature dependence of the decay

times calculated from a single exponential fit. The decay time changes from 10 ms at 10 K to less than 1 ms above 400 K. The initial change of the decay time with temperature can be attributed to an increase in the total radiative transition probability due to the thermal population of the excited vibrational states.[21-22] Above 400 K, the decay time reduces as accompanied by a decrease of luminescence intensity, signifying the onset of nonradiative quenching.

We modeled the temperature dependence of the luminescence decay time using the relation (3a) and data from Table S4 where τ(0) = 9 ms, with the result presented as a black curve in Figure 4b. We note that this theoretical calculation has no free parameters, using only parameters obtained experimentally from the low-temperature PL spectra ($\hbar\omega_v, \Omega_{dyn}^2(v)/\Omega_{stat}^2$). The theory reproduces the experimental data below 200 K, and we next applied the relation:[20]

$$\tau_E = \frac{\tau_T\left\{1+3\exp\left(\frac{-\Delta}{kT}\right)\right\}}{\left[1+\sum_v \frac{\Omega_{dyn}^2(v)}{\Omega_{stat}^2}\coth\left(\frac{\hbar\omega_v}{2kT}\right)\right]\left[\left(\frac{V_{S-O}}{\Delta'}\right)^2+3\exp\left(\frac{-\Delta}{kT}\right)\right]} \quad (5)$$

which considers the effect of admixing of the $^4T_{2g}$ and ^2E_g states due to spin-orbital interaction and thermal excitation of the Mn^{4+} from the ^2E_g to the $^4T_{2g}$ state, with the latter diminishing the luminescence lifetime due to the spin allowed $^4T_{2g} \rightarrow {}^4A_{2g}$ transition. V_{s-o} is the spin-orbit coupling constant and τ_T is the time constant interpreted as the radiative lifetime of the $^4T_{2g}$ state. The available experimental data for low field materials show that the $^4T_{2g} \rightarrow {}^4A_{2g}$ transition lifetime should be in the range 10-100 μs.[23] We obtain a good description of our experimental data (blue dashed curve in Figure 4) below 200 K using relation (5) with phonons parameters listed in Table S4 and $\tau_T = 0.1\ ms$ and $V_{so} = 215$ cm^{-1}. Additionally, we performed calculations using a simplified model with lattice phonons represented by the single phonon mode $\hbar\omega_{eff}$ given by the relation:

$$\tau_E = \frac{\tau_T\left\{1+3\exp\left(\frac{-\Delta}{kT}\right)\right\}}{\left[1+\frac{\Omega_{dyn}^2}{\Omega_{stat}^2}\coth\left(\frac{\hbar\omega_{eff}}{2kT}\right)\right]\left[\left(\frac{V_{S-O}}{\Delta\prime}\right)^2+3\exp\left(\frac{-\Delta}{kT}\right)\right]} \quad (5a)$$

The simplified model in (5a) reproduces the experimental data well at low temperatures for $\hbar\omega_{eff}$= 265 cm^{-1} , $\frac{\Omega_{dyn}^2}{\Omega_{stat}^2}$ =5.7, and $\tau_T = 0.1ms$, $V_{so} = 215$ cm^{-1}, as shown by the blue dashed dotted curve in Figure 4b. We note that the simplified effective phonon mode model produces a similar result to that using the more complete theory. We address the reduction in lifetime at temperature above 200 K by taking into account non-radiative processes by modification of relations (5) and (5a), obtaining the relation:

$$\tau_E{}' = \frac{\tau_T\left\{1+3\exp\left(\frac{-\Delta}{kT}\right)+\exp\left(\frac{-E_{nr}}{kT}\right)\right\}}{\left[1+\sum_v \frac{\Omega_{dyn}^{2(v)}}{\Omega_{stat}^2}\coth\left(\frac{\hbar\omega_v}{2kT}\right)\right][\left(\frac{V_{S-O}}{\Delta\prime}\right)^2+3\exp\left(\frac{-\Delta}{kT}\right)]+p_{nr}\cdot\tau_T\cdot\exp\left(\frac{-E_{nr}}{kT}\right)} \quad (6)$$

which considers all phonons, and relation:

$$\tau_E{}' = \frac{\tau_T\left\{1+3\exp\left(\frac{-\Delta}{kT}\right)+\exp\left(\frac{-E_{nr}}{kT}\right)\right\}}{\left[1+\frac{\Omega_{dyn}^2}{\Omega_{stat}^2}\coth\left(\frac{\hbar\omega_{eff}}{2kT}\right)\right][\left(\frac{V_{S-O}}{\Delta\prime}\right)^2+3\exp\left(\frac{-\Delta}{kT}\right)]+p_{nr}\cdot\tau_T\cdot\exp\left(\frac{-E_{nr}}{kT}\right)} \quad (6a)$$

which considers a single effective phonon.

In relations (6) and (6a), E_{nr} and p_{nr} are the activation energy and frequency factor (rate) for non-radiative processes, respectively. We performed calculations using the data from Table S4 in relation (6) with $\frac{\Omega_{dyn}^2}{\Omega_{stat}^2}$ = 5.7 and $\hbar\omega_{eff}$ = 265 cm^{-1} in relation (6a). These models describe the experimental data well, with that obtained from relation (6) shown as a solid red curve and from relation (6a) as a dotted red curve in Figure 4, with both yielding E_{nr} = 2900 cm^{-1} and p_{nr} = *12.6 10^8* s^{-1}. We note that E_{nr} is smaller than the energy of the $^4T_{2g}$ state, shown by Δ in Figure 2c. Therefore, we can tentatively attribute the non-radiative state excitation to ionization, which diminishes the number of electrons in the Mn ion, creating Mn^{5+}. Hence, Mn^{5+} + e^- should be

presented in the potential energy surface shown in Figure 2c, manifesting as parabola shifted to the left as a result of the diminished central ion - ligand distance (shown in red in Figure 2c).

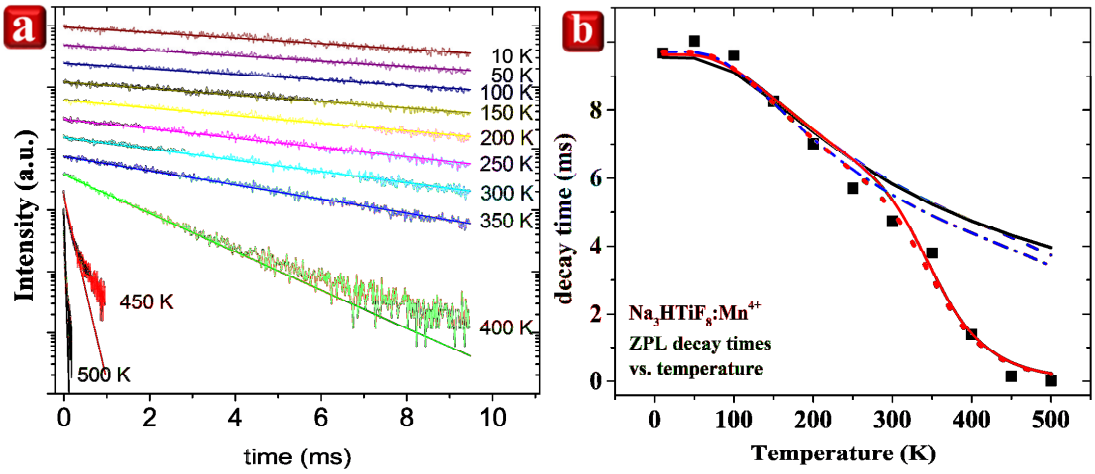

Figure 4. Temperature dependence of (a) ZPL decay profiles and (b) ZPL decay time under an excitation wavelength of 440 nm. Decay times were obtained by a single exponential decay fit (straight lines in (a)). The black curve is calculated using the relation (3), the blue dashed curve is calculated using the relation (5), the blue dashed-dotted curve is obtained using the relation (5a), the red solid curve is calculated using the relation (6), and the red curve is calculated using the relation (6a).

To evaluate the potential of the $Na_3HTiF_8:Mn^{4+}$ material series for practical applications, a blue-chip LED was fabricated using the β-SiAlON:Eu^{2+} and $Na_3HTi_{0.95}Mn_{0.05}F_8$ phosphors. The narrow-band emission of $Na_3HTiF_8:Mn^{4+}$ was observed in the electroluminescence spectra under the excitation as shown in Figure 5. The narrowband emission property makes it more suitable for the application in the backlighting system. The driving current was set to 0.02 A, which provided a luminous efficacy of 83.0 lm/W. In the Commission Internationale de l'˚clairage (CIE) 1931 color spaces, chromaticity coordinates (0.27,0.24) is close to the ideal backlighting color point (0.28,0.24). The generated area on the CIE diagram is around 91.4% of

NTSC area, which indicates that $Na_3HTiF_8:Mn^{4+}$ can be a potential candidate of red phosphors for the backlighting system in the future.

Moreover, we also evaluate the chemical and thermal stability of $Na_3HTiF_8:Mn^{4+}$. $Na_3HTi_{0.95}Mn_{0.05}F_8$ powders were put into an ethanol/water solution with a ratio of 2:3 as shown in Figure S3. $Na_3HTi_{1-x}Mn_xF_8$ maintained its strong luminescent intensity in the solution for 12 hr. To quantify its stability, we measure the relative luminescence intensity of the sample, which around 80% of its original intensity can be obtained after 12 hr. Also, the thermal property of $Na_3HTi_{0.95}Mn_{0.05}F_8$ is analyzed by the temperature-dependent photoluminescence as shown in Figure S4. We keep the sample for one minute for each data point to make sure the uniform temperature of the powder before measuring. The temperature for the backlighting system is around 400 K. $Na_3HTi_{1-x}Mn_xF_8$ can maintain 95% of its original luminescent intensity at 400 K, which can be a potential candidate for the backlighting-used phosphor materials.

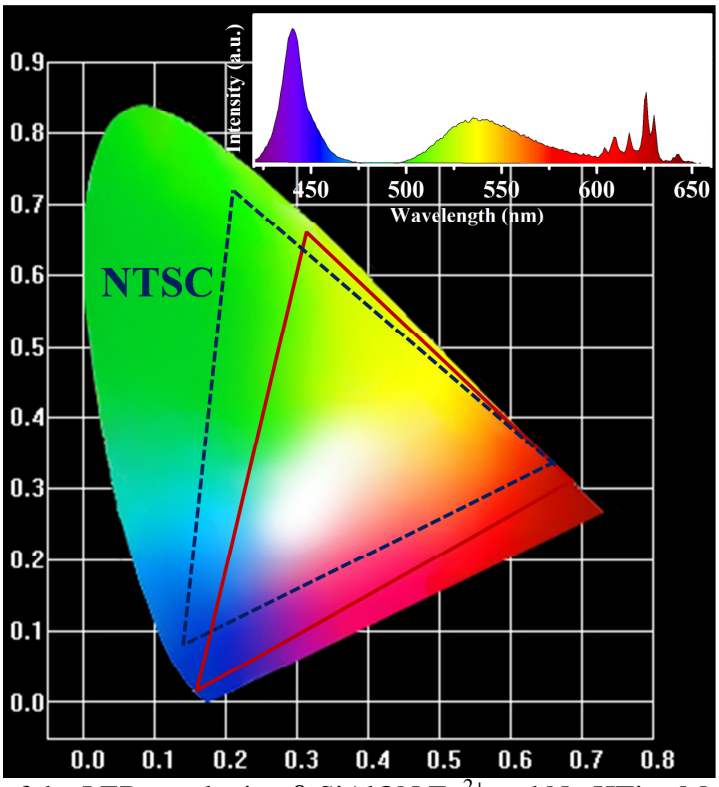

Figure 5. Color gamut of the LED employing β-SiAlON:Eu^{2+} and $Na_3HTi_{0.95}Mn_{0.05}F_8$ phosphors (Red triangle) compared with NTSC (dashed blue triangle). The inset figure is the electroluminescence (EL) spectrum of the fabricated LED.

In conclusion, a completely new series of Na_3HTiF_8:Mn^{4+} fluoride phosphors with high crystallinity are synthesized via a modified co-precipitation method. We use neutron powder diffraction to locate the H atom within the undoped parent of the series at the (0,1/2,0) position of the 4*b* crystallographic site within the *Cmcm* space group symmetry orthorhombic structure, resulting in a distortion of the octahedral TiF_6 unit, and impacting luminescence. Analysis of temperature-dependent photoluminescence and decay times considered three processes: (1) admixing of $^4T_{2g}$ and ^2E_g states due to spin-orbital interaction and thermal excitation of the Mn^{4+} from the ^2E_g to the $^4T_{2g}$ states, (2) the spin allowed $^4T_{2g} \rightarrow {}^4A_{2g}$ transition from thermal population, and (3) non-radiative processes. The given model described experimental data well and allowed the prediction of decay properties at low and high temperature, revealing the likely

presence of Mn^{5+} during the ionization process. A LED fabricated from a series member demonstrated the potential of the $Na_3HTiF_8:Mn^{4+}$ material series as candidates for backlighting system.

This study provides a new route for the synthesis of fluoride phosphors and demonstrates a good theoretical approach to predict the properties of the Mn^{4+} system, providing a path to address discrepancies between the theory and experiment of this class of materials.

ASSOCIATED CONTENT

SUPPORTING INFORMATION

The Supporting Information is available free of charge on the ACS Publications website at DOI: XXXX

Experimental methods; EDS data; SEM data; Quantum efficiency data; Temperature-dependent luminescent properties; Water-resistance.

AUTHOR INFORMATION

Corresponding Authors

*E-mails: wkpang@uow.edu.au (W.K.P), f10913@ntut.edu.tw (C.S.) and rsliu@ntu.edu.tw (R.S.L.)

Notes.

The authors declare no competing financial interest.
Mu-Huai Fang, Tsun-Hsiung Yang, and Tadeusz Lesniewski contribute equally to this paper.

ACKNOWLEDGMENTS

This work was supported by the Ministry of Science and Technology of Taiwan (Contract Nos. MOST 107-2113-M-002-008-MY3 and MOST 107-2923-M-002-004-MY3). This work was

supported by the National Centre for Research and Development Poland Grant (No. PL-TW/V/46/2018). T. Lesniewski would like to acknowledge the support of National Science Centre Poland, grant Preludium 13 (No. 2017/25/N/ST3/02412). The authors are grateful to the staff members at the Australian Centre for Neutron Scattering, ANSTO for their operations support. W. K. Pang would like to acknowledge the financial support from the Australian Research Council (ARC) through the Future Fellowship project (FT160100251) and the research funding from the University of Wollongong through the UIC International Links Grant Scheme 2018.

REFERENCES

(1) Wang, L.; Xie, R. J.; Suehiro, T.; Takeda, T.; Hirosaki, N. Down-Conversion Nitride Materials for Solid State Lighting: Recent Advances and Perspectives. *Chem. Rev.* **2018,** *118*, 1951-2009.
(2) Pust, P.; Schmidt, P. J.; Schnick, W. A Revolution in Lighting. *Nat. Mater.* **2015,** *14*, 454-458.
(3) Xia, Z.; Liu, Q. Progress in Discovery and Structural Design of Color Conversion Phosphors for LEDs. *Prog. Mater Sci.* **2016,** *84*, 59-117.
(4) Li, G.; Tian, Y.; Zhao, Y.; Lin, J. Recent Progress in Luminescence Tuning of Ce^{3+} and Eu^{2+}-Activated Phosphors for Pc-WLEDs. *Chem. Soc. Rev.* **2015,** *44*, 8688-8713.
(5) Uheda, K.; Hirosaki, N.; Yamamoto, Y.; Naito, A.; Nakajima, T.; Yamamoto, H. Luminescence Properties of a Red Phosphor, $CaAlSiN_3:Eu^{2+}$, for White Light-Emitting Diodes. *Electrochem. Solid-State Lett.* **2006,** *9*, H22-H25.
(6) Zeuner, M.; Pagano, S.; Schnick, W. Nitridosilicates and Oxonitridosilicates: From Ceramic Materials to Structural and Functional Diversity. *Angew. Chem. Int. Ed.* **2011,** *50*, 7754-7775.
(7) Höppe, H. A. Recent Developments in the Field of Inorganic Phosphors. *Angew. Chem. Int. Ed.* **2009,** *48*, 3572-3582.
(8) Oh, J. H.; Eo, Y. J.; Yoon, H. C.; Huh, Y. D.; Do, Y. R. Evaluation of New Color Metrics: Guidelines for Developing Narrow-Band Red Phosphors for WLEDs. *J. Mater. Chem. C* **2016,** *4*, 8326-8348.
(9) Takahashi, T.; Adachi, S. Mn^{4+}-Activated Red Photoluminescence in K_2SiF_6 Phosphor. *J. Electrochem. Soc.* **2008,** *155*, E183-E188.
(10) Xu, Y. K.; Adachi, S. Properties of $Na_2SiF_6:Mn^{4+}$ and $Na_2GeF_6:Mn^{4+}$ Red Phosphors Synthesized by Wet Chemical Etching. *J. Appl. Phys.* **2009,** *105*, 013525.
(11) Arai, Y.; Adachi, S. Optical Properties of Mn^{4+}-Activated Na_2SnF_6 and Cs_2SnF_6 Red Phosphors. *J. Lumin.* **2011,** *131*, 2652-2660.
(12) Xu, Y. K.; Adachi, S. Photoluminescence and Raman Scattering Spectra in $(NH_4)_2XF_6:Mn^{4+}$ (X= Si, Ge, Sn, and Ti) Red Phosphors. *J. Electrochem. Soc.* **2011,** *159*, E11-E17.
(13) Sekiguchi, D.; Nara, J.-i.; Adachi, S. Photoluminescence and Raman Scattering Spectroscopies of $BaSiF_6:Mn^{4+}$ Red Phosphor. *J. Appl. Phys.* **2013,** *113*, 183516.
(14) Zhu, H.; Lin, C. C.; Luo, W.; Shu, S.; Liu, Z.; Liu, Y.; Kong, J.; Ma, E.; Cao, Y.; Liu, R. S. Highly Efficient Non-Rare-Earth Red Emitting Phosphor for Warm White Light-Emitting Diodes. *Nat. Commun.* **2014,** *5*, 4312.

(15) Wu, W. L et al. High Color Rendering Index of $Rb_2GeF_6:Mn^{4+}$ for Light-Emitting Diodes. *Chem. Mater.* **2017,** *29*, 935-939.
(16) Xi, L.; Pan, Y.; Zhu, M.; Lian, H.; Lin, J. Abnormal Site Occupancy and High Performance in Warm WLEDs of a Novel Red Phosphor, $NaHF_2:Mn^{4+}$, Synthesized at Room Temperature. *Dalton Trans.* **2017,** *46*, 13835-13844.
(17) Fang, M. H. et al. Control of Luminescence via Tuning of Crystal Symmetry and Local Structure in Mn^{4+}-Activated Narrow Band Fluoride Phosphors. *Angew. Chem. Int. Ed.* **2018,** *57*, 1797 –1801.
(18) Tanabe, Y.; Sugano, S. On the Absorption Spectra of Complex Ions II. *J. Phys. Soc. Jpn.* **1954,** *9*, 766-779.
(19) Henderson, B.; Imbusch, G. F. *Optical Spectroscopy of Inorganic Solids*, Oxford University Press: 2006; Vol. 44.
(20) Reisfeld, M. J.; Matwiyoff, N. A.; Asprey, L. B. The Electronic Spectrum of Cesium Hexafluoromanganese (IV). *J. Mol. Spectrosc.* **1971,** *39*, 8-20.
(21) Lesniewski, T.; Mahlik, S.; Grinberg, M.; Liu, R. S. Temperature Effect on the Emission Spectra of Narrow Band Mn^{4+} Phosphors for Application in LEDs. *PCCP* **2017,** *19*, 32505-32513.
(22) Grinberg, M.; Lesniewski, T.; Mahlik, S.; Liu, R. S. $3d^3$ System–Comparison of Mn^{4+} and Cr^{3+} in Different Lattices. *Opt. Mater.* **2017,** *74*, 93-100.
(23) Wojtowicz, A.; Grinberg, M.; Lempicki, A. The Coupling of $^4T_2$ and ^2E States of the Cr^{3+} Ion in Solid State Materials. *J. Lumin.* **1991,** *50*, 231-242.